International Journal of Heat and Mass Transfer 127 (2018) 1084–1094

Contents lists available at ScienceDirect

International Journal of Heat and Mass Transfer

journal homepage: www.elsevier.com/locate/ijhmt

Fusion zone geometries, cooling rates and solidification parameters during wire arc additive manufacturing

W. Ou [a,b], T. Mukherjee [a], G.L. Knapp [a], Y. Wei [b], T. DebRoy [a,*]

[a] Department of Materials Science and Engineering, The Pennsylvania State University, University Park, PA 16802, USA
[b] Department of Material Science and Technology, Nanjing University of Aeronautics and Astronautics, Jiangsu 210016, China

ARTICLE INFO

Article history:
Received 14 May 2018
Received in revised form 17 July 2018
Accepted 23 August 2018

Keywords:
Wire arc additive manufacturing
Heat transfer and fluid flow
Cooling rates
Solidification parameters
H13 tool steel

ABSTRACT

Structure, properties and serviceability of components made by wire arc additive manufacturing (WAAM) depend on the process parameters such as arc power, travel speed, wire diameter and wire feed rate. However, the selection of appropriate processing conditions to fabricate defect free and structurally sound components by trial and error is expensive and time consuming. Here we develop, test and utilize a three-dimensional heat transfer and fluid flow model of WAAM to calculate temperature and velocity fields, deposit shape and size, cooling rates and solidification parameters. The calculated fusion zone geometries and cooling rates for various arc power and travel speed and thermal cycles considering convective flow of molten metal agreed well with the corresponding experimental data for H13 tool steel deposits. It was found that convection is the main mechanism of heat transfer inside the molten pool. Faster travel speed enhanced the cooling rate but reduced the ratio of temperature gradient to solidification growth rate indicating increased instability of plane front solidification of components. Higher deposition rates could be achieved by increasing the heat input, using thicker wires and rapid wire feeding.

1. Introduction

Wire arc additive manufacturing (WAAM) is developed from arc welding and suitable for making large components because of high deposition rates, low equipment and feedstock costs [1]. WAAM involves melting of wire by the arc, transfer of molten metal droplets to a molten pool, convective flow of liquid metal inside the molten pool driven by surface tension gradient [2–4], deformation of the molten pool surface by arc pressure and solidification of the molten pool [2,3]. These physical phenomena govern the temperature and velocity distributions, deposit shape and size, and the structure and properties of the components. In addition, transient and spatially non-uniform temperature field results in residual stresses and distortion [5–8]. Therefore, fabrication of a structurally sound and defect free WAAM component requires precise control of the process by appropriate selection of the process variables such as arc power, travel speed, wire diameter and wire feed rate. However, selection of these variables by trial and error is expensive, time consuming and provides no guarantee of achieving the desired structure and properties. A recourse is to develop, test and utilize a mathematical framework that can serve as a basis for selecting appropriate process conditions based on scientific principles.

WAAM has already been successfully applied for making components of steels [7,9,10], aluminum alloys [11,12], titanium alloys [13,14] and nickel alloys [15] and several attempts have been made to model the process. Analytical models have been used to predict build geometry [16,17] and surface topology [18]. However, these models are based on empirical formulae and ignore the heat and mass transfer during the process. Heat conduction models have also been used to calculate temperature distribution [19,20], temperature gradient [21] and residual stresses [19]. However, these models neglect the convective flow of liquid metal inside the molten pool that often dominates the heat transfer mechanism inside the molten pool. Manvatkar et al. [22] and Arrizubieta et al. [23] noted that calculations neglecting the convective heat transfer significantly overestimate the peak temperature and cooling rates. Svensson et al. [24] mentioned that the heat conduction calculations are inadequate to accurately calculate the cooling rates. Volume of fluid (VOF) based numerical models used by Silwal et al. [25] consider the molten metal convection and have been used to predict the deposit geometry. However, these models are computationally expensive and have not been used to estimate essential metallurgical variables such as temperature gradient, cooling rates and solidification parameters. What is needed and currently not available is a well-tested comprehensive phenomenological

* Corresponding author.
E-mail address: debroy@psu.edu (T. DebRoy).

https://doi.org/10.1016/j.ijheatmasstransfer.2018.08.111
0017-9310/

model of WAAM capable of calculating the essential metallurgical variables for different process variables.

Here we develop, test and use a three-dimensional heat transfer and fluid flow model of wire arc additive manufacturing to calculate the temperature and velocity fields, deposit shape and size, cooling rates and solidification parameters for a single-track deposit. Experiments are conducted by depositing H13 tool steel at different arc powers and travel speeds to validate the model. The variations of fusion zone geometry with power and travel speed are compared with the corresponding experimental results. Calculated temperature variation with time is also tested against independent experimental data. After validation, the model is used to quantitatively study the effects of a wide variety of process variables such as arc power, travel speed, wire feed rate and wire diameter on different metallurgical variables.

2. Theoretical model

2.1. Assumptions

The following simplifying assumptions are made to make the numerical calculations involving heat and fluid flow, droplet transfer and molten pool surface geometry tractable.

(1) The liquid metal is assumed to be a Newtonian fluid and its viscosity depends on temperature and pressure [26]. The Boussinesq approximation is used for the calculation of buoyancy driven flow [6].
(2) Effective thermal conductivity and viscosity of the liquid metal are enhanced to account for turbulent convection effects [27]. No separate turbulence models are used to estimate turbulent components of transport properties.
(3) Because the arc current in the WAAM process is higher than 100 A, metal transfer mode is assumed to be globular-type [28]. Due to difficulties with the measurement, droplet temperature is calculated based on net heat balance [29]. The droplet velocity is calculated considering arc plasma effect using the formula provided by Kumar and Bhaduri [30].

2.2. Solution domain

The three-dimensional solution domain for a single-track deposit is shown in Fig. 1. Calculations are done in the Cartesian coordinate system, which is attached to the heat source. In other words, the arc source and the molten pool are stationary in space, and the substrate material enters and leaves the computational domain at the scanning speed. Half of the solution domain is considered in the calculations by taking advantage of symmetry. Droplets impinge on the molten pool to form a deposit, and their sensible heat is considered as a volumetric heat source for the heat transfer calculations [29]. The surface of the deposit is assumed to be flat during the calculation of the temperature and velocity fields. After the calculation, the free surface profile of the deposit is estimated by minimizing the total surface energy on the top surface of the deposit [31]. Finally, the grids are adjusted to fit the surface profile, and the temperature and velocity fields are then reassigned in the fitted grid system.

2.3. Governing equations

The heat transfer and fluid flow model solves the equations of conservation of mass, momentum and energy in three components along the x, y, and z directions [32,33].

$$\frac{\partial(\rho u_i)}{\partial x_i} = 0 \tag{1}$$

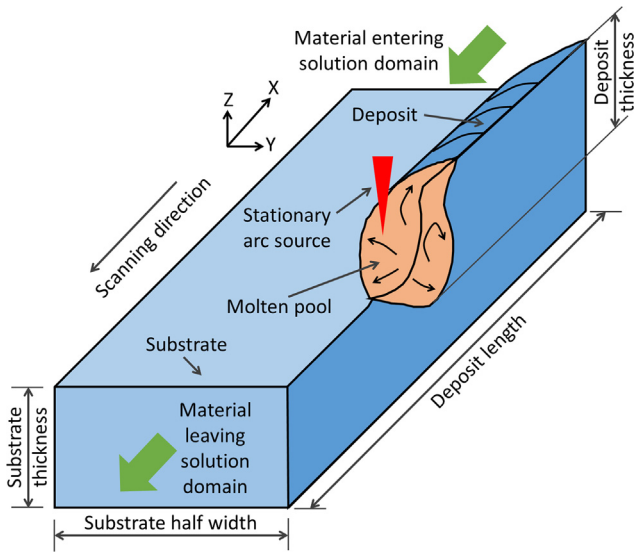

Fig. 1. Schematic of the solution domain consisting of molten pool, substrate and deposit. The dimensions are given in Table 2. Scanning direction is along negative X-axis. Half of the solution domain is used because of the symmetry with respect to XZ-plane.

$$\frac{\partial(\rho u_j u_i)}{\partial x_i} = \frac{\partial}{\partial x_i}\left(\mu \frac{\partial u_j}{\partial x_i}\right) + S_j \tag{2}$$

$$\frac{\partial(\rho u_i h)}{\partial x_i} = \frac{\partial}{\partial x_i}\left(\frac{k}{C_P}\frac{\partial h}{\partial x_i}\right) - \rho U_S \frac{\partial h}{\partial x_i} + S_L + S_V \tag{3}$$

where ρ is the density, u_i and u_j are the velocity components along the i- and j-directions, respectively, and x_i is the distance along the i-direction, μ is the effective viscosity, and S_j is a source term for the momentum equation (2) including buoyancy force, the motion of the heat source, electromagnetic force and frictional dissipation in the mushy zone. These source terms were described in detail by Zhang et al. [31] and Mundra et al. [34]. The symbol h is the sensible heat, C_P is the specific heat, k is the thermal conductivity, U_S is the scanning speed, S_L is the source term that accounts for latent heat and S_V is the source term for the additional heat from metal droplets. The source term S_V is calculated assuming that the heat energy from the metal droplets is distributed uniformly in a cylindrical cavity inside the work piece [29,34,35]. Detail derivation of the source term S_V is presented in Appendix A. The thermophysical properties of the alloys are provided in Table 1 [36,37].

Table 1
Thermo-physical properties of AISI 1040 steel, H13 steel, and ER70S-6 steel [36,37]. Arc efficiencies are estimated following Haelsig et al. [44].

Properties	AISI 1040	H13	ER70S-6
Liquidus temperature (K)	1745	1585	1712
Solidus temperature (K)	1800	1725	1766
Thermal conductivity of solid (W/mK)	25.3	30.4	33.0
Thermal conductivity of liquid (W/mK)	34.0	31.0	35.4
Enhanced thermal conductivity of liquid, (W/mK)	253.0	304.0	283.3
Specific heat of solid (J/kg K)	696.3	734.3	701.3
Specific heat of liquid (J/kg K)	700.4	823.4	902.5
Density (kg/m^3)	7290	7800	7700
Viscosity (kg/m s)	6.4×10^{-3}	5.7×10^{-3}	5.7×10^{-3}
Enhanced viscosity, (kg/m s)	29.6×10^{-3}	105×10^{-3}	26.4×10^{-3}
$d\gamma/dT$ (N/m K)	-0.40×10^{-3}	-0.43×10^{-3}	-0.41×10^{-3}
Arc efficiency	0.67	0.67	0.82

2.4. Boundary conditions

On the top surface, the boundary conditions for the energy conservation equation include the heat flux from the arc source and convective and radiative heat losses. The net heat flux (J_h) on the top surface is expressed as:

$$J_h = \frac{(IV\eta - H_d)}{2\pi r_b^2}\exp\left(-\frac{x^2+y^2}{2r_b^2}\right) - \varepsilon\sigma(T^4 - T_a^4) - h(T - T_a) \quad (4)$$

where the 1st, 2nd and 3rd term on the right hand side of the equation represent the heat flux from the arc source, radiative loss and convective loss, respectively. The arc source heat flux is assumed to have Gaussian power density distribution where I is the arc current, V is the arc voltage, η is the arc efficiency, H_d is the heat content of the droplet (see Appendix A), r_b is the arc radius, x and y are the distances from the arc axis. In the convective and radiative heat loss terms ε is the emissivity, σ is the Stefan-Boltzmann constant, T is the top surface temperature, and h is the heat transfer coefficient. Convective and radiative heat losses are also applied to the rest of the top-surface of the computational domain.

Spatial gradient of the surface tension on the top surface of the molten pool results in a shear stress called Marangoni stress, τ [3,5]. It is expressed as:

$$\tau_i = \frac{d\gamma}{dT}\frac{dT}{dr} = \mu\frac{du}{dz} \quad (5)$$

where the suffix 'i' denotes x or y directions, T is the temperature, u is velocity of the liquid metal on the top surface of the molten pool, γ is the surface tension, μ is the viscosity and r is the radial distance from the axis of the heat source. The resulting velocities along x and y-directions generated due to this shear stress are applied as boundary conditions of the momentum conservation equation on the top surface of the liquid pool.

Since, there is no heat transfer across the symmetry plane (y = 0), the boundary condition for the enthalpy calculation is applied as, $\frac{\partial h}{\partial y} = 0$. Boundary conditions for velocity calculations at that plane are $\frac{\partial u}{\partial y} = 0$, $v = 0$ and $\frac{\partial w}{\partial y} = 0$ where u, v and w are the components of velocity in the x, y and z-directions, respectively.

2.5. Geometry of the deposit surface

Total energy on the surface of the molten pool includes the surface energy, potential energy in the gravitational field, arc pressure displacing the pool surface and work performed by the arc pressure and droplet impact displacing the pool surface. The arc pressure (P_a) depends on total arc force on the top surface of the molten pool and is assumed to have Gaussian distribution [38]. Average droplet impact force on the top surface of the molten pool depends on droplet mass, velocity and transfer frequency [39]. The pressure due to the droplet impact (P_d) is essentially the impact force per unit area and is assumed to have Gaussian distribution on the top surface of the molten pool [39]. The molten pool surface profile is obtained by solving the following equation [31]:

$$P_a + P_d + \lambda + \gamma\frac{(1+\phi_y^2)\phi_{xx} - 2\phi_x\phi_y\phi_{xy} + (1+\phi_x^2)\phi_{yy}}{(1+\phi_x^2+\phi_y^2)^{3/2}} = \rho g\phi \quad (6)$$

where γ is the surface tension coefficient of the liquid, Φ is the configuration function of the molten pool surface and λ is the Lagrangian multiplier, which is obtained from the following volume continuity equation:

$$\iint \phi dxdy - v_d = 0 \quad (7)$$

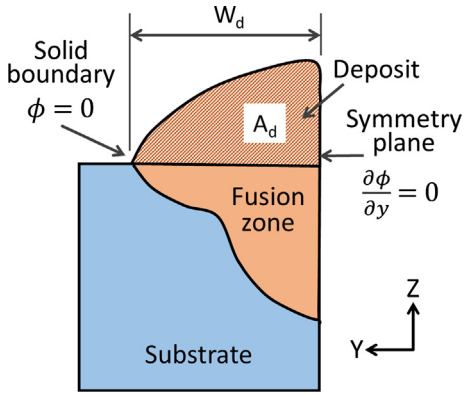

Fig. 2. Schematic of the transverse section of the deposit. Half of the deposit is considered because of the symmetry with respect to XZ-plane.

where v_d is the volume of the material deposited per unit time. The symbols ϕ_x, ϕ_{xx} and ϕ_{xy} are defined as: $\phi_x = \frac{\partial\phi}{\partial x}$, $\phi_{xx} = \frac{\partial\phi_x}{\partial x}$ and $\phi_{xy} = \frac{\partial\phi_y}{\partial x}$, respectively. The definitions for Φ_y and Φ_{yy} are similar. The boundary conditions of total surface energy and solution method of Lagrangian multiplier are described by Zhang et al [31].

The cross-sectional area of the deposit is shown in Fig. 2. Similar to Zhang et al. [31], the cross-sectional area (A_d) considering only half of the deposit is expressed as:

$$A_d = \frac{\pi r_w^2 w_f}{2U_S} \quad (8)$$

where r_w is the radius of the filler wire, w_f is wire feed rate and U_S is the scanning speed. The configuration function of the surface profile ϕ is calculated by solving the overall mass conservation equations [31]:

$$\lambda + \gamma\frac{\phi_{yy}}{(1+\phi_y^2)^{3/2}} = \rho g\phi \quad (9)$$

$$\int_0^{W_d}\phi dy - A_d = 0 \quad (10)$$

Eq. (10) represents the deposit surface profile (ϕ) by considering that amount of liquid metal distributes over a distance of W_d (half of the pool width). The boundary conditions (shown in Fig. 2) used in the calculation of solidified surface profiles are given as: $\phi = 0$ at the solid boundary and $\frac{\partial\phi}{\partial y} = 0$ at the symmetry plane (y = 0).

2.6. Solution method

The entire solution domain is divided into small control volumes. For a 120 mm long deposit the total number of grids is 102 × 92 × 44 (length × width × height). A control volume method has been implemented for the discretization of the governing equations [40]. The SIMPLE algorithm [40] is used to solve the governing equations and the calculations are completed using an in-house Fortran code. Typically, around 3.5 million linear equations and 6,000 iteration steps are solved for the deposition, which takes approximately 10 minutes in a personal computer with 2.8 Gigahertz i7 processor and 8 Gigabyte random access memory (RAM).

3. Experimental investigation

A series of 120 mm long single-track builds using H13 tool steel wire are deposited on a 250 mm × 150 mm × 4 mm AISI 1040 steel substrate. The heat source of WAAM was a custom-designed Pana-

Table 2
The WAAM process variables used in experiments and simulations.

	Current (A)	Voltage (V)	Speed (mm/s)	Wire feed rate (mm/s)	Wire diameter (mm)	Substrate dimension (mm)
Experiment	100–200	18–22	5–11.7	63–143	1.2	250 × 150 × 4
Figs. 3–5	200	22	5	83	1.2	320 × 360 × 17
Fig. 6	200	22	11.7	133	1.2	320 × 360 × 17
Fig. 7	200	22	5–11.7	68–143	1.2	320 × 360 × 17
Fig. 8	100–200	18–22	5	63	1.2	320 × 360 × 17
Fig. 9a	200	22	5, 11.7	83, 143	1.6	400 × 340 × 10
Fig. 9b	250	30	10	60	1.6	400 × 340 × 10
Fig. 10	250	15	8.3	60–100	1.0–1.36	320 × 360 × 17
Fig. 11a	200–300	15	8.3	80	1.2	320 × 360 × 17
Fig. 11b	150	20	5–11.7	80	1.2	320 × 360 × 17
Fig. 11c	250	15	8.3	60–100	1.2–1.36	320 × 360 × 17
Fig. 12a	200–300	15	8.3	80	1.2	320 × 360 × 17
Fig. 12b	150	20	5–11.7	80	1.2	320 × 360 × 17
Fig. 12c	250	15	8.3	60–100	1.2–1.36	320 × 360 × 17

sonic digital MIG/MAG welding power source, which was inverter controlled using direct current (DC) with output current range from DC 30 A to 350 A and output voltage range from DC 12 V to 31.2 V. The specimens were fabricated using a welding robot combined with control box, workbench and wire feed system. The 6-axis independent movements of the robot are programed and controlled by a software-based control system. The deposited builds were protected by high purity argon with 15 L/min gas flow rate. The samples were ground and polished using colloidal silica and subsequently were etched using the standard Keller's reagent (2.5 mL HNO_3 + 1.5 mL HCL + 1 mL HF + 95 mL H_2O) for 20 s. The process conditions used in these experiments are provided in Table 2.

4. Results and discussions

Fig. 3(a) shows the three-dimensional temperature and velocity fields during the fabrication of a single-track H13 steel deposit. Due to the rapid scanning, the molten pool extends along the opposite direction of the arc source movement. Fig. 3(b) shows the magnified view of the temperature and velocity fields close to the molten pool. The two-phase region containing both liquid and solid material, commonly called the mushy zone, is bounded by the solidus temperature (1585 K) and liquidus temperature (1725 K) isotherms. During solidification, the characteristics of the mushy zone play an important role in solidification morphology. The region within the liquidus isotherm is called the fusion zone. Molten metal velocities are shown by black arrows whose magnitude can be estimated by comparing their lengths with the reference vector provided.

Liquid metal motion in the molten pool is driven mainly by the surface tension gradients and to a much lesser extent by the buoyancy force. Due to the negative value of $d\gamma/dT$, the liquid metal flows from the center to the periphery on the top surface of the molten pool. The liquid metal is depressed in the middle of the pool due to the strong arc pressure and droplet impinging force. This flow pattern allows more heat transfer from the heat source to the bottom of the molten pool, which, in turn, results in deep penetration. Fig. 3 also depicts the free surface deformation of the molten pool. The liquid metal is pushed to the rear part of the molten pool and forms the crown as it solidifies.

Fig. 4(a) shows the temperature and velocity fields at different transverse sections of the deposit. Near the leading edge of the deposit, the molten pool is depressed due to arc and droplet forces and the fusion zone has finger-like (*i.e.* deep and narrow) penetration in to the substrate. Towards the rear end of the molten pool, the arc and droplet forces acting on the surface decrease, resulting in a crown geometry determined largely by surface tension forces. Fig. 4(b) and (c) show the stream traces on two transverse planes at two different distances along the distance of the arc travel. Under the arc, the surface depression combined with surface tension gradients leads to two separate convection loops, as shown by the stream traces in section 1 of Fig. 4(b). Behind the arc, the circulation of the molten metal is slower due to the reduced temperature gradients, as shown in section 2 of Fig. 4(c).

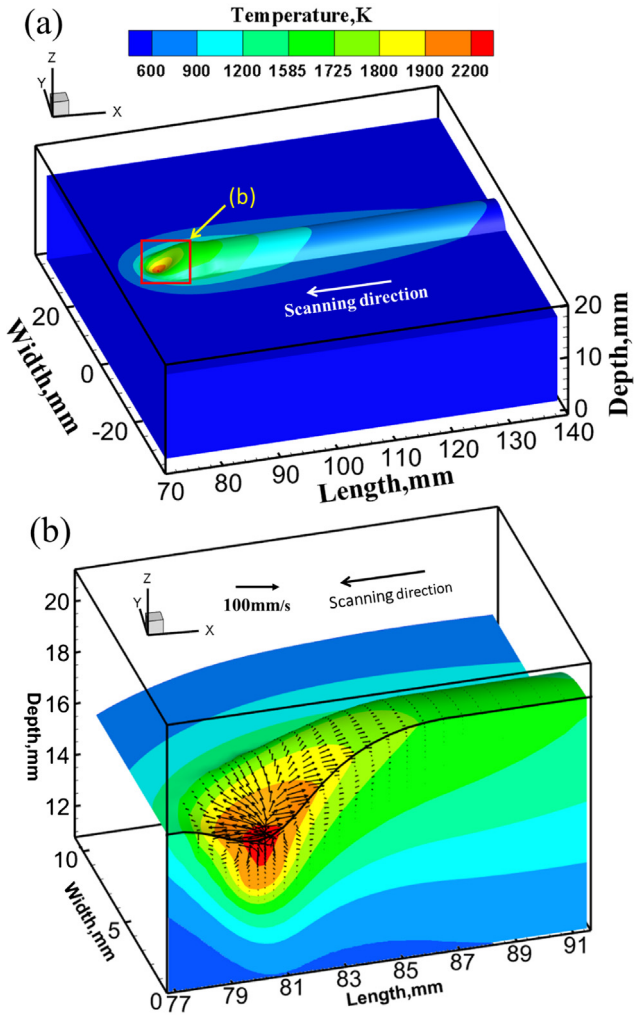

Fig. 3. (a) Calculated temperature and velocity fields for a single track H13 deposition using process parameters given in Table 2. (b) Magnified views of temperature fields in (a).

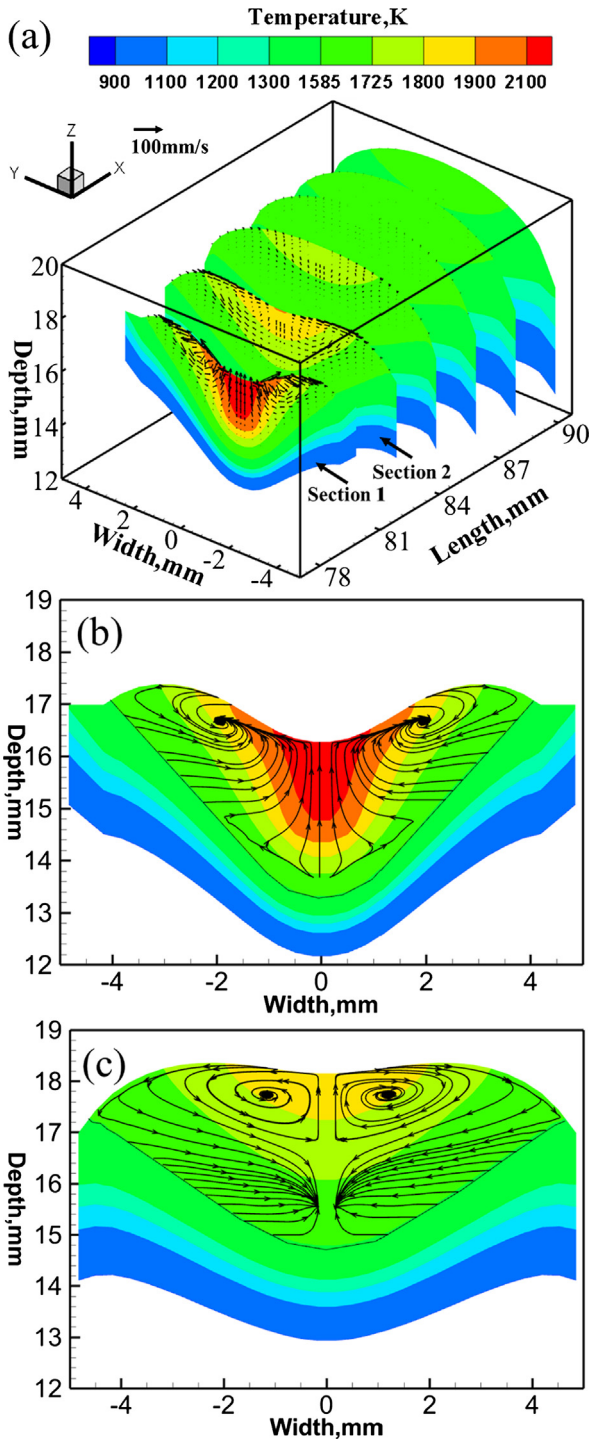

Fig. 4. (a) Temperature and velocity fields at different transverse planes. Temperature fields and stream traces of molten metal flow at two transverse sections (b) section 1 (under the arc) and (c) section 2 (behind the arc) shown in figure (a). All plots use the process parameters given in Table 2.

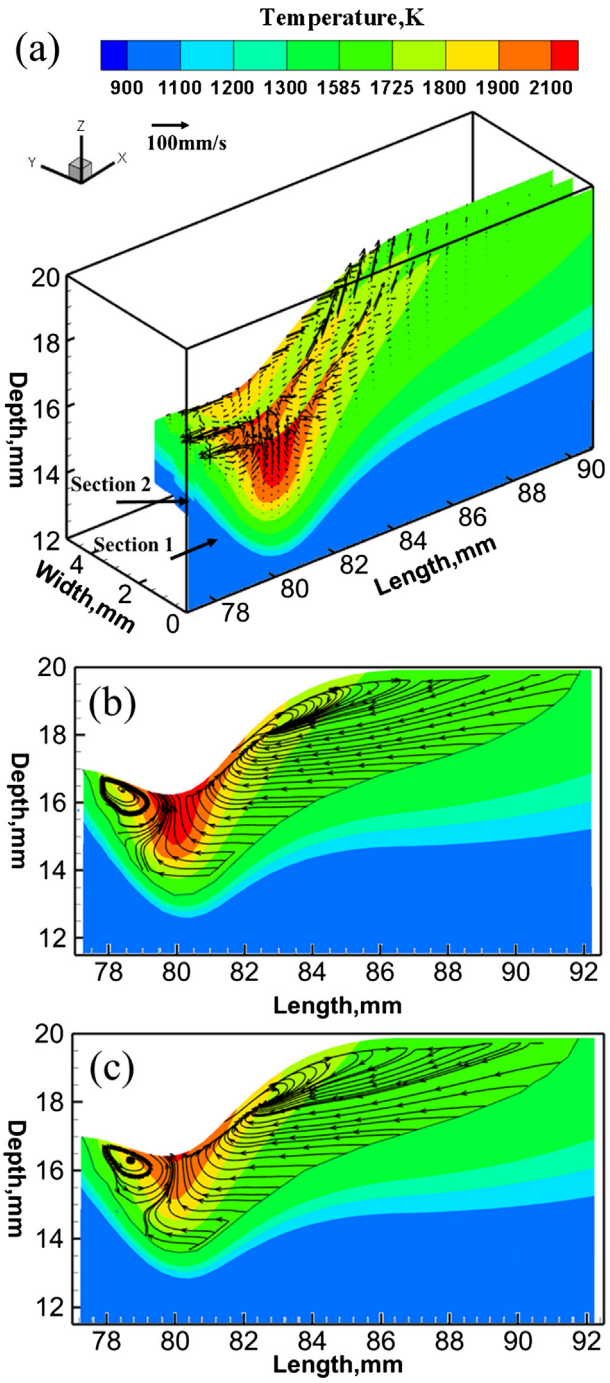

Fig. 5. (a) Temperature and velocity fields at different longitudinal planes. Temperature fields and stream traces of molten metal flow at two longitudinal sections (b) section 1 (under the arc) and (c) section 2 (right side of the arc) shown in figure (a). All plots use the process parameters given in Table 2.

Temperature and velocity fields for longitudinal sections at different distances from the arc center are shown in Fig. 5(a). Comparing the two sections in Fig. 5(b) and (c), there little difference in the distribution of temperatures and velocities. Stream traces for both sections reveal a small convection loop in the front of the molten pool and a larger convection loop in the rear of the pool. Because the pool is longer than it is wide, the temperature gradient from the peak temperature at the center of the pool to the liquidus isotherm at the edge of the pool is larger in the width direction than the length direction. This results in a higher surface tension gradient near the front of the pool and lower surface tension gradient in the rear, correlating to the magnitude of the velocities.

Mukherjee et al. [41] used the dimensionless Péclet number (*Pe*) to describe the ratio of heat transferred by convection to the heat transferred by conduction during additive manufacturing,

$$Pe = \frac{LU}{k/\rho c_p} \tag{11}$$

where ρ is the density of the fluid, c_p is the specific heat of the fluid, k is the thermal conductivity, U is the characteristic velocity (maximum velocity inside the pool), and L is the characteristic length (width of the molten pool). For the simulations shown in Figs. 3–5, the computed values of the Péclet number are approximately 100. A Péclet number significantly greater than one indicates that convection of molten metal dominates the heat transfer inside the molten pool [41]. Fig. 6 shows a comparison between the experimentally observed transverse cross-section (in YZ-plane) of the deposit with that of the computed values considering and ignoring convective heat transfer. When the calculation is done ignoring convection, the width of the pool is 13% smaller than the experimental value. This is because the radially outward flow of liquid metal carries heat to increase the width of the molten pool. Therefore, the deposit width is underestimated when the convective flow is ignored. In addition, the heat that should have been transported radially is now concentrated in the middle of the pool and a portion of it goes downwards, resulting in an overestimation of the penetration depth of the fusion zone. Thus, the calculations that neglect the mixing of hot and cold liquid inside the molten pool cannot predict the correct geometry of the deposit.

Two of the most influential and easily controllable variables in WAAM are the arc power and travel speed. The roles of these variables on the fusion zone geometry are examined both experimentally and theoretically in Figs. 7 and 8. Fig. 7(a–c) shows the effects of varying travel speed. The cross-section of the fusion zone decreases in size with increasing travel speed in both the theoretical calculations and the experimentally observed results. This is because of the lower heat input per unit length at faster scanning speed. Fig. 8(a–c) shows that the deposit sizes and fusion zone dimensions increase with arc power, which increases the heat input per unit length.

Fig. 9(a) shows the temperature variation with time monitored at the mid-height and mid-length of the deposit center while fabricating a single track H13 deposit. The peak temperature corresponds with the time the arc source reaches the monitoring location. At 11.7 mm/s scanning speed, the peak temperature is observed at around 2.6 s. However, at a slower traveling speed of 5 mm/s the peak temperature is observed at about 6 s, because the arc source takes a longer time to reach the monitoring location. Heating takes place rapidly as the arc approaches the monitoring location. However, once heated, cooling is comparatively slower because of the time needed for the transport of heat throughout the molten pool and into the substrate. During cooling, there is a sudden change in slope between the liquidus (1725 K) and solidus

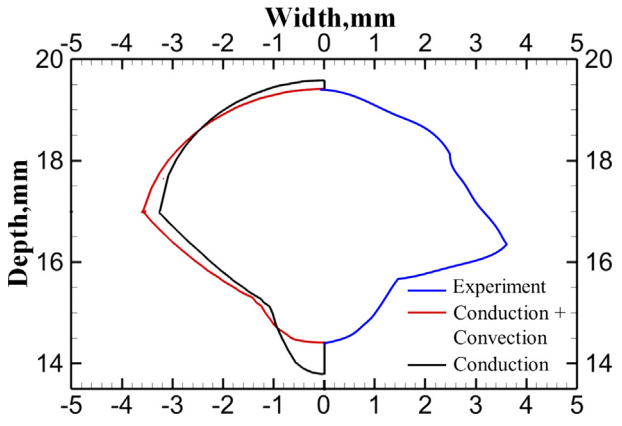

Fig. 6. Comparison between the calculated transverse section of the H13 deposit considering and neglecting molten metal convection with the corresponding experimentally measured macrograph. The results are obtained using the process parameters given in Table 2.

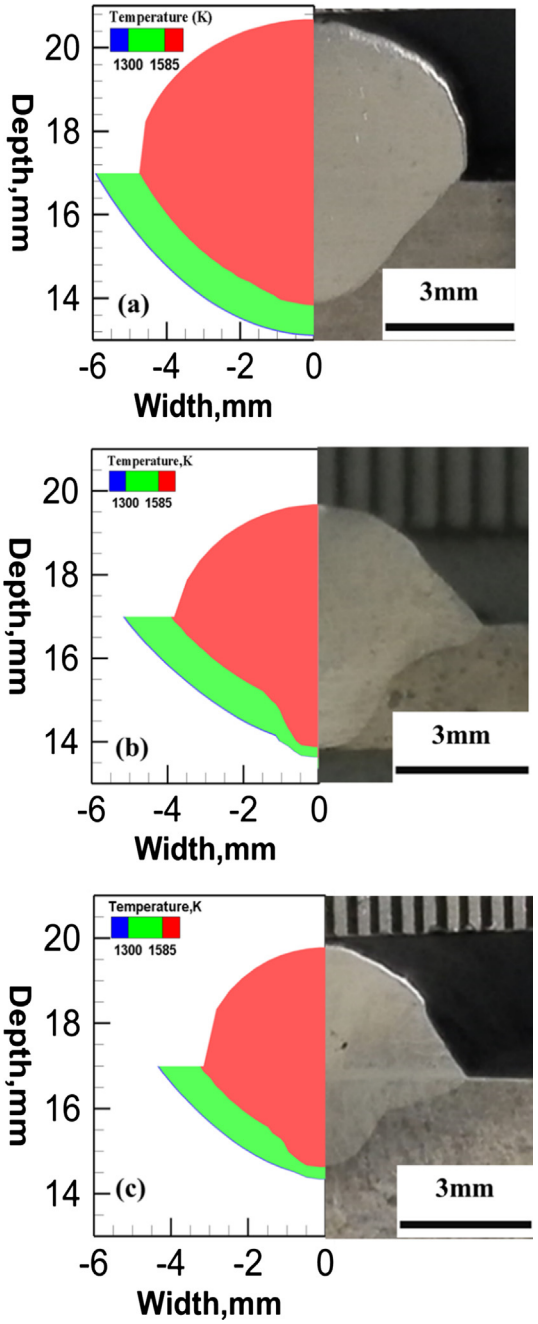

Fig. 7. Comparison between the calculated transverse sections of the H13 deposit with the corresponding experimentally measured macrograph using (a) 5 mm/s (b) 8.3 mm/s and (c) 11.7 mm/s scanning speed. Other process parameters are given in Table 2. The red region bounded by the solidus temperature (1585 K) isotherm represents the transverse section of the deposit.

(1585 K) temperatures because of the liquid-to-solid phase transformation and the release of latent heat during solidification. Fig. 9(b) compares the computed temperature variation with time during the deposition of ER70S-6 steel to the corresponding experimental results of Bai et al. [20]. Temperatures were measured with an IR camera during the experiment. The slight mismatch between the experimental and numerical results is likely due to the difficulties in the temperature measurement during deposition, as well as several assumptions made during modeling.

The agreement of the calculated fusion zone geometry for various travel speeds (Fig. 7) and arc powers (Fig. 8), as well as agree-

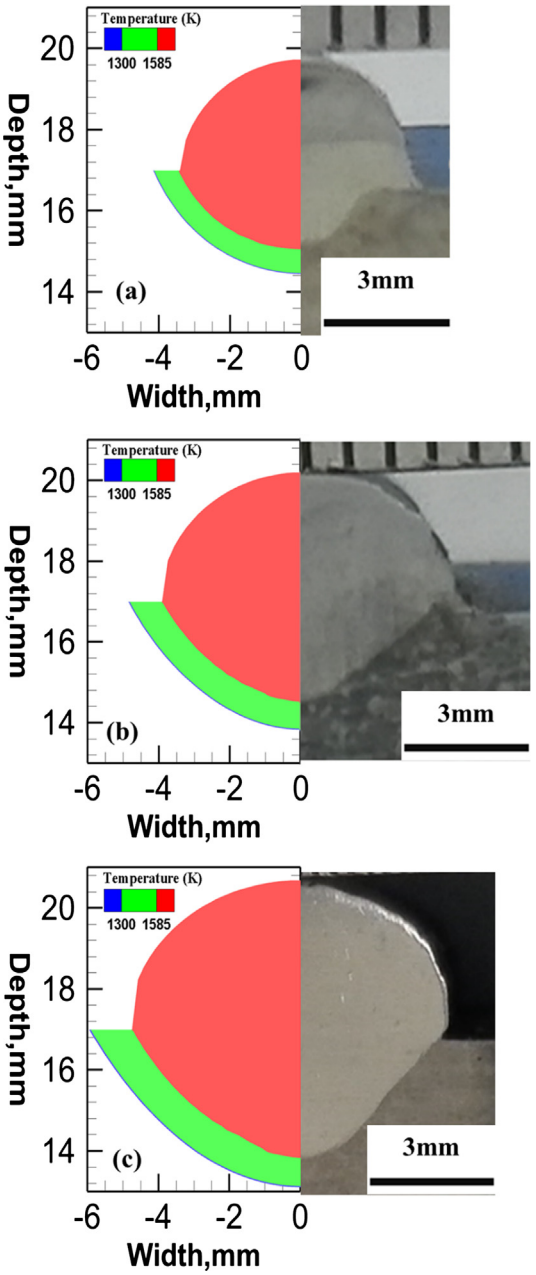

Fig. 8. Comparison between the calculated transverse sections of the H13 deposit with the corresponding experimentally measured macrograph using (a) 1800 W (b) 3000 W and (b) 4400 W arc power. Other process parameters are given in Table 2. The red region bounded by the solidus temperature (1585 K) isotherm represents the transverse section of the deposit.

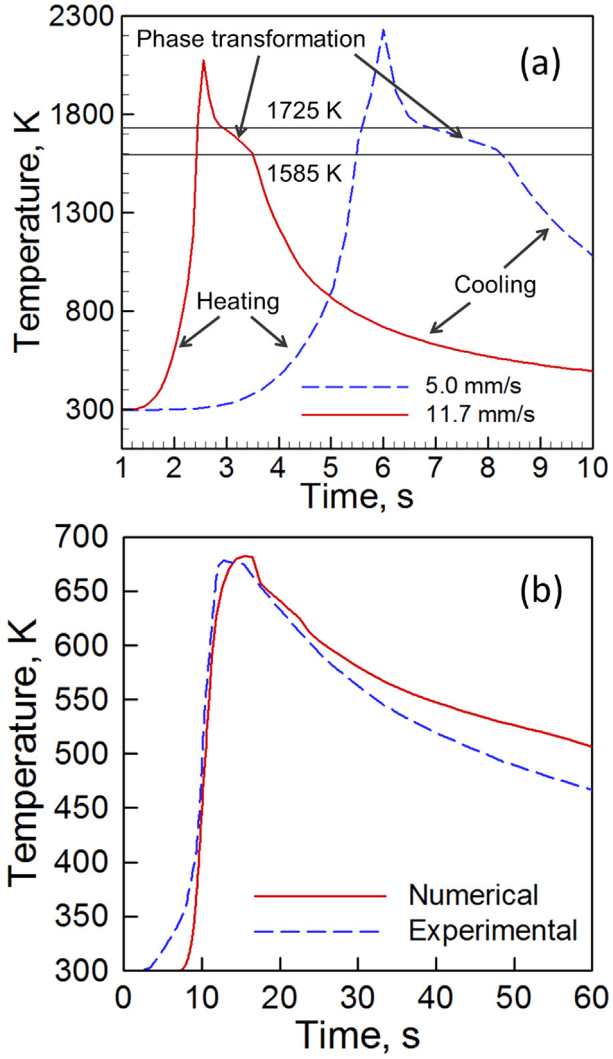

Fig. 9. (a) Temperature variation with time monitored at the mid height and mid-length of the deposit center while fabricating a single track H13 deposit using two different scanning speeds. The process parameters are given in Table 2. (b) Comparison between the calculated and the experimentally measured thermal cycles [20].

ment of thermal cycles (Fig. 9(b)) with corresponding experimental data provides confidence in using the model to investigate the roles of important process parameters on deposit shape and size, temperature fields, cooling rates and solidification parameters.

Fig. 10(a–c) shows the effects of wire feed rate and wire diameter on fusion zone width, penetration depth and deposit height, respectively. The fusion zone width is primarily controlled by available heat energy for melting and convective flow within the molten pool. As evident from Figs. 7 and 8, width depends largely on arc power and scanning speed. For a constant heat input, fusion zone width does not change significantly with wire feed rate and wire diameter as shown in Fig. 10(a). However, the enhanced mass flow rate that results from higher wire feed rate and larger wire diameter increases the heat transfer from the arc source to the bottom of the molten pool. Therefore, penetration depth increases with both wire feed rate and wire diameter as shown in Fig. 10 (b). Fig. 10(c) shows that the deposit height increases with both wire feed rate and wire diameter because of an increase in the amount of material deposited per unit time.

The temperature gradient, G, and the growth rate of the solidification front, R, provide important information about the solidification morphology. The value of G across the mushy zone is relevant during solidification, as it drives the solidification kinetics. In steady state, R along the centerline is equivalent to the travel speed and varies spatially by the angle of the pool boundary relative to the centerline. The product of G and R, GR, represents the cooling rate, which is linked to the scale of the microstructure. Fig. 11(a–c) shows the variation of cooling rate during solidification calculated at mid-length and mid-height of the deposit for various arc powers, travel speeds, wire feed rates and wire diameters. Convective flow of liquid metal inside the molten pool mixes the hot and cold liquid and reduces the temperature gradient inside the pool. Therefore, heat conduction calculations that neglect the molten metal convection overestimate the temperature gradient and cooling rate as shown in Fig. 11(a) and (b). By increasing linear heat input, higher

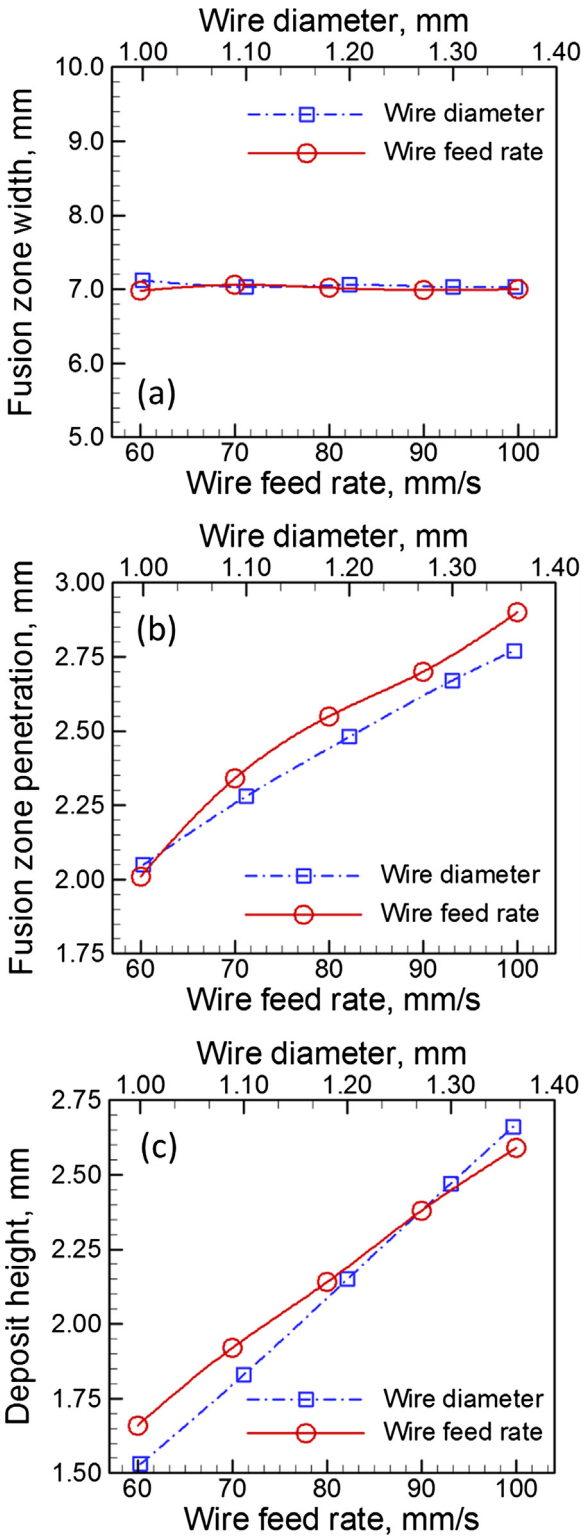

Fig. 10. Effects of wire feed rate and wire diameter on (a) fusion zone width (b) penetration depth and (c) deposit height of a single track H13 deposit. Graphs are plotted using the process parameters given in Table 2. Variations with respect to wire diameter and wire feed rate are plotted at 80 mm/s wire feed rate and 1.2 mm wire diameter, respectively.

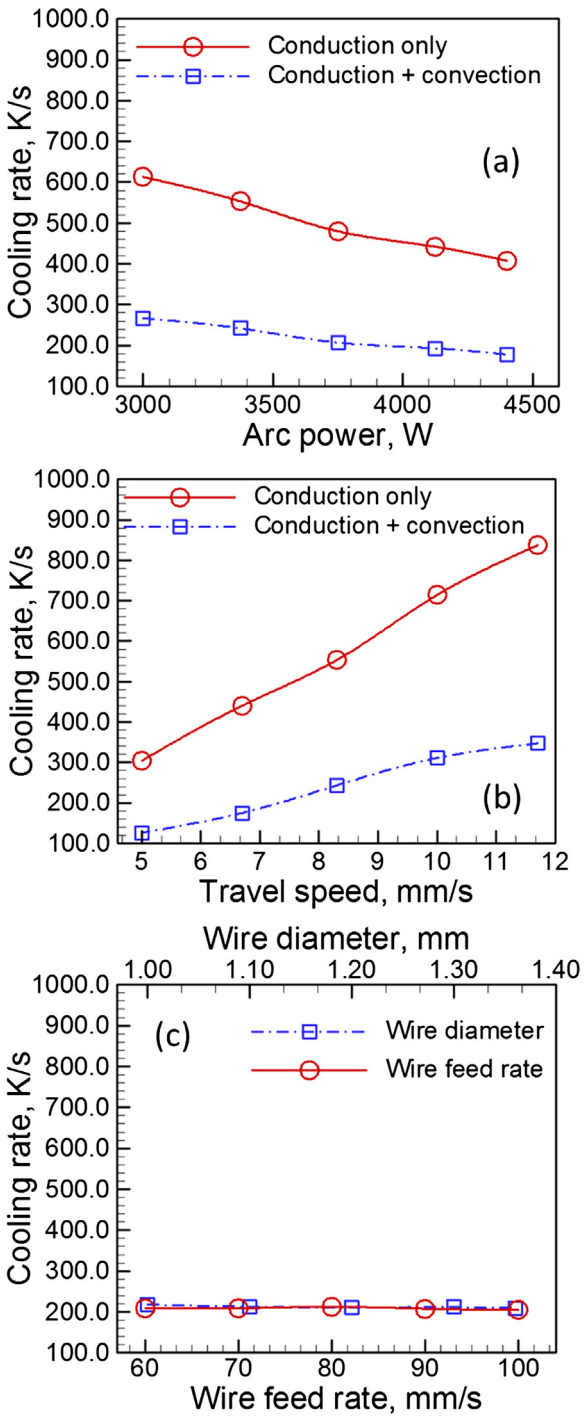

Fig. 11. Variations of cooling rate during solidification with respect to (a) arc power (b) travel speed and (c) wire feed rate and wire diameter. Cooling rates are calculated at the mid height and mid-length of the deposit center while fabricating a single track H13 deposit. Graphs are plotted using the process parameters given in Table 2. Variations with respect to wire diameter and wire feed rate are plotted at 80 mm/s wire feed rate and 1.2 mm wire diameter, respectively.

arc power and slow scanning speed result in more molten material that cools and solidifies relatively slowly. Computed results in Fig. 11(a) and (b) support this, showing cooling rates increasing as arc power increases and scanning speed decreases. Wire feed rate and wire diameter do not significantly affect the heat transfer from the molten pool to the substrate, because they do not change the amount of heat input into the system. Therefore, the cooling rate remains almost unchanged for different wire feed rates and wire diameters, as shown in Fig. 11(c).

Dividing G by R gives the solidification parameter G/R, which is necessary for determining solidification morphology. High values of G/R indicate stable plane front solidification, while low values

indicate unstable growth. The constitutional supercooling criterion for plane front solidification is represented as:

$$G/R \geqslant \Delta T_E/D_L \tag{12}$$

where ΔT_E is the range of equilibrium solidification temperatures (140 K for H13 tool steel) and D_L is the solute diffusion coefficient (2×10^{-2} mm^2 s^{-1} for carbon in liquid iron [42]). Therefore, calculated value of $\Delta T_E/D_L$ for H13 tool steel is 7×10^3 K s mm^2. Fig. 12(a–c) shows the variation of G/R during solidification, calculated at mid-length and mid-height of the deposit, with arc power, travel speed, wire feed rate and wire diameter. Notably, all the values for G/R are significantly lower than the critical value of 7×10^3 K s mm^2 required for plane-front solidification. Therefore, formation of either cellular or dendritic solidification structure is expected and observed in experimental results. Conduction calculations neglecting convective flow of molten metal result in higher G/R values, because larger temperature gradients develop due to the lack of mixing of hot and cold liquids. Wider and longer molten pools at higher arc powers also result in lower temperature gradients. Therefore, G/R decreases with arc power as shown in Fig. 12(a). Growth rate of the solidification front increases with travel speed, so G/R decreases with travel speed as shown in Fig. 12(b). Since, wire feed rate and wire diameter do not significantly affect the heat transfer from the molten pool to the substrate, G/R remains almost unchanged with these two parameters, as shown in Fig. 12(c). If in-depth analysis of microstructural features is desired, then the effects of convective fluid flow, travel speed, and arc power must be considered to obtain accurate solidification parameters. In all cases presented here, either cellular or dendritic solidification morphology occurs, with variations in GR affecting the scale of the microstructure.

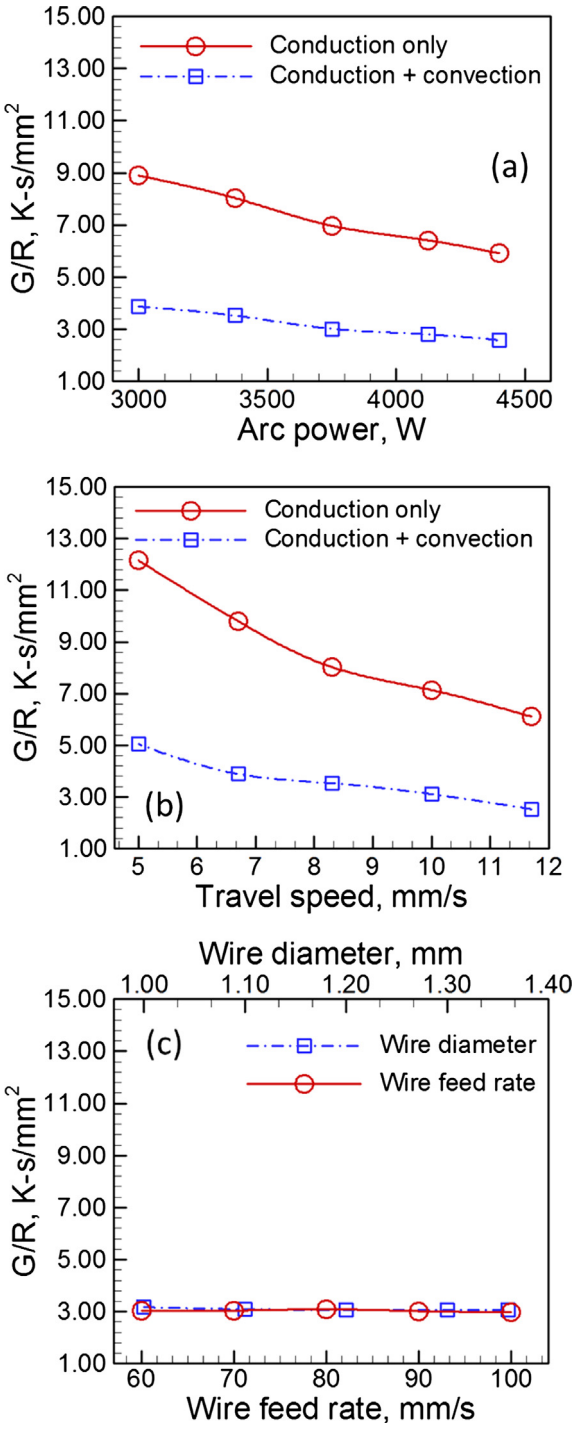

Fig. 12. Variations of G/R ratios during solidification with respect to (a) arc power (b) travel speed and (c) wire feed rate and wire diameter. G/R ratios are calculated at the mid height and mid-length of the deposit center while fabricating a single track H13 deposit. Graphs are plotted using the process parameters given in Table 2. Variations with respect to wire diameter and wire feed rate are plotted at 80 mm/s wire feed rate and 1.2 mm wire diameter, respectively.

5. Summary and conclusions

A three-dimensional heat transfer and fluid flow model of wire arc additive manufacturing was developed, tested and used to the calculate temperature and velocity fields, deposit shape and size, cooling rates and solidification parameters for a single-track H13 tool steel deposit. Effects of arc power, travel speed, wire feed rate and wire diameter on different metallurgical variables were examined. Below are the specific findings.

(1) The calculated dimensions of fusion zones and thermal cycles for various arc powers and travel speeds agreed well with the corresponding experimental results.
(2) Droplet impact force and arc pressure resulted in deep finger penetration under the arc. The liquid metal depressed under the arc was displaced to the rear end of the molten pool and formed a crown. The resulting wide and deep deposits facilitate high deposition rates that make the WAAM process a practical choice for rapid production of large components at low cost.
(3) Convection is the main mechanism of heat transfer inside the molten pool. Heat conduction calculations ignoring convection in the pool result in inaccurate deposit geometries and unrealistically high cooling rates. In contrast, convective heat transfer calculations provide reliable results of cooling rates and deposit geometry.
(4) The low values of the ratio of temperature gradient (G) to solidification growth rate (R) indicated high instability of plane front solidification in wire arc additive manufacturing. Since wire feed rate and wire diameter did not directly affect the heat transfer from the molten pool, the cooling rate and G/R did not change significantly by altering those two process parameters. However, a faster cooling rate and higher G/R could be obtained by reducing heat input per unit length.
(5) Higher heat input achieved by slow scanning or higher arc power resulted in larger deposits. Use of thicker wire and rapid wire feeding also increased deposit size because of higher amount of material deposition under those conditions.

Conflict of interest

There is no conflict of interest.

Acknowledgement

The authors gratefully acknowledge a project funded by the Priority Academic Program Development of Jiangsu Higher Education Institutions (PAPD) and the financial support of the Fundamental Research Funds for the Central Universities NP2016204. One of the authors (T.M.) acknowledges support of an American Welding Society research fellowship, grant number 179466.

Appendix A

The heat energy from the metal droplets is assumed to be distributed uniformly in a cylindrical cavity inside the work piece. Therefore, the source term S_V in the energy conservation equation (Eq. (3)) is calculated as below [30]:

$$S_V = \frac{H_d}{\pi h_e r_e^2} \tag{A1}$$

where H_d is the heat content of the droplet, h_e and r_e are the effective height and radius of the cylindrical cavity. Heat content of the droplets is calculated as [29]:

$$H_d = \rho\pi r_w^2 w_f [C_P(T_d - T_a) + \Delta H] \tag{A2}$$

where ρ is the density of the material, r_w is wire radius, w_f is wire feed rate, C_P is specific heat, T_d is the droplet temperature, T_a is the ambient temperature and ΔH is latent heat.

The effective height (h_e) and radius (r_e) of the cylindrical cavity in Eq. (A1) are expressed as [29]:

$$r_e = a \tag{A3}$$

$$h_e = h_c - x + a \tag{A4}$$

where x is the distance traveled by the center of mass of the cylinder, a is the droplet diameter and h_c is the height of the cavity.

The droplet diameter (a) in Eqs. (A3) and (A4) depends on the electrode diameter and arc current [29].

The height of the cavity (h_c) in equation A4 is calculated by equating the total work done in creating the cavity (W) and the kinetic energy of drop (KE). The total work done in creating the cavity (W) consists of work done against the hydrostatic pressure and creating a new surface and is represented as [30]:

$$W = \int_0^{h_c} (pdV + 2\pi a\gamma dH) \tag{A5}$$

where γ is the coefficient surface tension, H denotes the height, V and p denote the volume and the hydrostatic pressure of the cylindrical cavity, respectively. The volume and hydrostatic pressure are represented as [30]:

$$V = \pi a^2 h_c \tag{A6}$$

$$p = \rho g h_c \tag{A7}$$

Combining Eqs. (A5)–(A7), the total work done in creating the cavity, W, can be obtained as:

$$W = \pi a\left(\frac{1}{2}a\rho g h_c^2 + 2\gamma h_c\right) \tag{A8}$$

The kinetic energy of drop is expressed as:

$$KE = \frac{1}{2} m v_d^2 \tag{A9}$$

where m is the droplet mass depends on droplet diameter (a) and density (ρ) and v_d is the velocity of droplets [43]. Therefore, by equating the total work done in creating the cavity (W) and the kinetic energy of drop (KE), the cavity height (h_c) can be calculated as:

$$h_c = \left(-\frac{2\gamma}{a\rho g} + \sqrt{\left[\left(\frac{2\gamma}{a\rho g}\right)^2 + \frac{a v_d^2}{6g}\right]}\right) \tag{A10}$$

The distance traveled by the center of mass of the cylinder (x) in Eq. (A4) is calculated by solving the acceleration equation of droplets [30]:

$$\frac{d^2x}{dt^2} = \left(g + \frac{2\gamma}{a\rho h_c}\right) - \frac{g}{h_c}x \tag{A11}$$

where g is the acceleration due to gravity. By solving this equation,

$$x = \left(h_c + \frac{2\gamma}{a\rho g}\right)\left\{1 - \cos\left[\left(\frac{g}{h_c}\right)^{1/2} t\right]\right\} \tag{A12}$$

where t is the time that is inverse to the droplet frequency (D). The droplet frequency (D) depends on wire feed rate (w_f), wire radius (r_w) and droplet diameter (a) and is represented as:

$$D = \frac{\pi r_w^2 w_f}{\frac{1}{6}\pi a^3} \tag{A13}$$

References

[1] T. DebRoy, H.L. Wei, J.S. Zuback, T. Mukherjee, J.W. Elmer, J.O. Milewski, A.M. Beese, A. Wilson-Heid, A. De, W. Zhang, Additive manufacturing of metallic components–process, structure and properties, Prog. Mater. Sci. 92 (2018) 112–224.
[2] S.A. David, T. DebRoy, Current issues and problems in welding science, Science 257 (5069) (1992) 497–502.
[3] T. DebRoy, S.A. David, Physical processes in fusion welding, Rev. Mod. Phys. 67 (1) (1995) 85.
[4] H.L. Wei, J. Mazumder, T. DebRoy, Evolution of solidification texture during additive manufacturing, Sci. Rep. 5 (2015) 16446.
[5] T. Mukherjee, J.S. Zuback, A. De, T. DebRoy, Printability of alloys for additive manufacturing, Sci. Rep. 6 (2016) 19717.
[6] G.L. Knapp, T. Muhkerjee, J.S. Zuback, H.L. Wei, T.A. Palmer, A. De, T. DebRoy, Building blocks for a digital twin of additive manufacturing, Acta Mater. 135 (2017) 390–399.
[7] J. Ding, P. Colegrove, J. Mehnen, S. Ganguly, P.S. Almeida, F. Wang, S. Williams, Thermo-mechanical analysis of wire and arc additive layer manufacturing process on large multi-layer parts, Comput. Mater. Sci. 50 (12) (2011) 3315–3322.
[8] T. Mukherjee, V. Manvatkar, A. De, T. DebRoy, Mitigation of thermal distortion during additive manufacturing, Scripta Mater. 127 (2017) 79–83.
[9] S.W. Williams, F. Martina, A.C. Addison, J. Ding, G. Pardal, P. Colegrove, Wire + arc additive manufacturing, Mater. Sci. Technol. 32 (7) (2016) 641–647.
[10] J. Xiong, R. Li, Y. Lei, H. Chen, Heat propagation of circular thin-walled parts fabricated in additive manufacturing using gas metal arc welding, J. Mater. Process. Technol. 251 (2018) 12–19.
[11] B. Cong, J. Ding, S. Williams, Effect of arc mode in cold metal transfer process on porosity of additively manufactured Al-6.3% Cu alloy, Int. J. Adv. Manuf. Technol. 76 (9–12) (2015) 1593–1606.
[12] J. Gu, B. Cong, J. Ding, S. Williams, Y. Zhai, Wire + arc additive manufacturing of aluminium, Proceedings of the 25th Annual International Solid Freeform Fabrication Symposium, Austin, TX, 2014, pp. 451–458.
[13] F. Wang, S. Williams, M. Rush, Morphology investigation on direct current pulsed gas tungsten arc welded additive layer manufactured Ti6Al4V alloy, Int. J. Adv. Manuf. Technol. 57 (5–8) (2011) 597–603.
[14] J. Zhang, X. Wang, S. Paddea, X. Zhang, Fatigue crack propagation behaviour in wire + arc additive manufactured Ti-6Al-4V: effects of microstructure and residual stress, Mater. Des. 90 (2016) 551–561.
[15] D. Ding, Z. Pan, S. van Duin, H. Li, C. Shen, Fabricating superior nial bronze components through wire arc additive manufacturing, Materials 9 (8) (2016) 652.
[16] H. Geng, J. Xiong, D. Huang, X. Lin, J. Li, A prediction model of layer geometrical size in wire and arc additive manufacture using response surface methodology, Int. J. Adv. Manuf. Technol. 93 (1–4) (2017) 175–186.
[17] D. Ding, Z. Pan, D. Cuiuri, H. Li, A multi-bead overlapping model for robotic wire and arc additive manufacturing (WAAM), Rob. Comput. Integr. Manuf. 31 (2015) 101–110.

[18] Y. Li, Y. Sun, Q. Han, G. Zhang, I. Horváth, Enhanced beads overlapping model for wire and arc additive manufacturing of multi-layer multi-bead metallic parts, J. Mater. Process. Technol. 252 (2018) 838–848.
[19] J. Ding, P. Colegrove, J. Mehnen, S. Williams, F. Wang, P. Sequeira Almeida, A computationally efficient finite element model of wire and arc additive manufacture, Int. J. Adv. Manuf. Technol. 70 (1–4) (2014) 227–236.
[20] X. Bai, H. Zhang, G. Wang, Improving prediction accuracy of thermal analysis for weld-based additive manufacturing by calibrating input parameters using IR imaging, Int. J. Adv. Manuf. Technol. 69 (5–8) (2013) 1087–1095.
[21] J. Xiong, Y. Lei, R. Li, Finite element analysis and experimental validation of thermal behavior for thin-walled parts in GMAW-based additive manufacturing with various substrate preheating temperatures, Appl. Therm. Eng. 126 (2017) 43–52.
[22] V. Manvatkar, A. De, T. DebRoy, Heat transfer and material flow during laser assisted multi-layer additive manufacturing, J. Appl. Phys. 116 (12) (2014) 124905.
[23] J.I. Arrizubieta, A. Lamikiz, F. Klocke, S. Martínez, K. Arntz, E. Ukar, Evaluation of the relevance of melt pool dynamics in Laser Material Deposition process modeling, Int. J. Heat Mass Transf. 115 (2017) 80–91.
[24] L.E. Svensson, B. Gretoft, H.K.D.H. Bhadeshia, An analysis of cooling curves from the fusion zone of steel weld deposits, Scand. J. Metall 15 (97) (1986) e103.
[25] B. Silwal, M. Santangelo, Effect of vibration and hot-wire gas tungsten arc (GTA) on the geometric shape, J. Mater. Process. Technol. 251 (2018) 138–145.
[26] R.B. Bird, W.E. Stewart, E.N. Lightfoot, Transport Phenomena 2002, John Wiley & Sons, New York, 2004.
[27] A. De, T. DebRoy, A smart model to estimate effective thermal conductivity and viscosity in the weld pool, J. Appl. Phys. 95 (9) (2004) 5230–5240.
[28] J.F. Lancaster, The Physics of Welding, International Institute of Welding, Pergamon, Oxford, 1986.
[29] Z. Yang, T. DebRoy, Modeling macro-and microstructures of gas-metal-arc welded HSLA-100 steel, Metall. Mater. Trans. B 30 (3) (1999) 483–493.
[30] S. Kumar, S.C. Bhaduri, Theoretical investigation of penetration characteristics in gas metal-arc welding using finite element method, Metall. Mater. Trans. B 26 (3) (1995) 611–624.
[31] W. Zhang, C.H. Kim, T. DebRoy, Heat and fluid flow in complex joints during gas metal arc welding—part I: numerical model of fillet welding, J. Appl. Phys. 95 (9) (2004) 5210–5219.
[32] T. Mukherjee, W. Zhang, T. DebRoy, An improved prediction of residual stresses and distortion in additive manufacturing, Comput. Mater. Sci. 126 (2017) 360–372.
[33] T. Mukherjee, J.S. Zuback, W. Zhang, T. DebRoy, Residual stresses and distortion in additively manufactured compositionally graded and dissimilar joints, Comput. Mater. Sci. 143 (2018) 325–337.
[34] K. Mundra, T. DebRoy, K.M. Kelkar, Numerical prediction of fluid flow and heat transfer in welding with a moving heat source, Numer. Heat Transf., Part A Appl. 29 (2) (1996) 115–129.
[35] M. Ushio, C.S. Wu, Mathematical modeling of three-dimensional heat and fluid flow in a moving gas metal arc weld pool, Metall. Mater. Trans. B 28 (3) (1997) 509–516.
[36] K.C. Mills, Recommended Values of Thermophysical Properties for Selected Commercial Alloys, Woodhead Publishing, 2002.
[37] P. Ferro, H. Porzner, A. Tiziani, F. Bonollo, The influence of phase transformations on residual stresses induced by the welding process—3D and 2D numerical models, Modell. Simul. Mater. Sci. Eng. 14 (2) (2006) 117.
[38] H.B. Smartt, AMS Handbook, ASM International, 1993, p. 27.
[39] Z.N. Cao, P. Dong, Modeling of GMA weld pools with consideration of droplet impact, J. Eng. Mater. Technol. 120 (4) (1998) 313–320.
[40] S. Patankar, Numerical Heat Transfer and Fluid Flow, CRC Press, 1980.
[41] T. Mukherjee, V. Manvatkar, A. De, T. DebRoy, Dimensionless numbers in additive manufacturing, J. Appl. Phys. 121 (6) (2017) 064904.
[42] V. Manvatkar, A. De, T. DebRoy, Spatial variation of melt pool geometry, peak temperature and solidification parameters during laser assisted additive manufacturing process, Mater. Sci. Technol. 31 (8) (2015) 924–930.
[43] W.G. Essers, R. Walter, Heat transfer and penetration mechanisms with GMA and plasma-GMA welding, Weld. J. 60 (2) (1981) 37–42.
[44] A. Haelsig, M. Kusch, P. Mayr, Calorimetric analyses of the comprehensive heat flow for gas metal arc welding, Weld. World 59 (2015) 191–199.